



This is a repository copy of *Tensile stress-strain characteristics of rubberised concrete from flexural tests*.

White Rose Research Online URL for this paper:
<http://eprints.whiterose.ac.uk/154393/>

Version: Accepted Version

Article:

Wang, Z., Hu, H. orcid.org/0000-0003-1786-9485, Hajirasouliha, I. orcid.org/0000-0003-2597-8200 et al. (2 more authors) (2020) Tensile stress-strain characteristics of rubberised concrete from flexural tests. *Construction and Building Materials*, 236. 117591. ISSN 0950-0618

<https://doi.org/10.1016/j.conbuildmat.2019.117591>

Article available under the terms of the CC-BY-NC-ND licence
(<https://creativecommons.org/licenses/by-nc-nd/4.0/>).

Reuse

This article is distributed under the terms of the Creative Commons Attribution-NonCommercial-NoDerivs (CC BY-NC-ND) licence. This licence only allows you to download this work and share it with others as long as you credit the authors, but you can't change the article in any way or use it commercially. More information and the full terms of the licence here: <https://creativecommons.org/licenses/>

Takedown

If you consider content in White Rose Research Online to be in breach of UK law, please notify us by emailing eprints@whiterose.ac.uk including the URL of the record and the reason for the withdrawal request.



eprints@whiterose.ac.uk
<https://eprints.whiterose.ac.uk/>

Tensile Stress-Strain Characteristics of Rubberised Concrete from Flexural Tests

Zhao Wang^{1*}, Hang Hu², Iman Hajirasouliha³, Maurizio Guadagnini⁴, Kypros Pilakoutas⁵,

Abstract: The tensile characteristics of rubberised concrete are practically impossible to obtain from direct tensile tests, due to the non-uniform distribution of aggregates and stiffness. In this paper, notched three-point bending tests are used to characterise Mode I fracture behaviour of concrete incorporating high volume of rubber particles obtained from post-consumer tyres. The test results show that rubber particles enhance energy absorption capacity and ductility of concrete. Inverse finite element analysis is performed to indirectly determine tensile stress-strain curves of rubberised concrete. The key material parameters introduced in the constitutive model are tensile strength, fracture energy and crack band width. The spurious mesh dependency is resolved by adopting a simple modification to the softening modulus as a function of element size. The performance of the proposed tensile stress-strain relation is compared with that of Model Code 2010 using ABAQUS concrete damaged plasticity model and shows considerably better accuracy. The proposed model can be used to improve the reliability of numerical analyses of rubberised concrete elements and structures.

Author keywords: Rubberised concrete; Three-point bending test; Fracture energy; Tension softening; Inverse finite element analysis; Crack band.

1. Introduction

Vulcanised rubber material extracted from end-of-life tyres is highly durable, has good strength and deformability, and can maintain its volume under stress, thus making it an ideal candidate to replace mineral aggregate for highly

¹ PhD candidate. Dept. of Civil and Structural Engineering, The University of Sheffield, Sir Frederick Mappin Building, Mappin Street, Sheffield, S1 3JD, UK. Email (corresponding author*): zwang88@sheffield.ac.uk

² PhD. Chengdu Communication Investment Corporation, 66 Shenghe 1st Road, Chengdu City, Sichuan Province, China. Postcode: 610041. huhang750@hotmail.com

³ Senior Lecturer. Dept. of Civil and Structural Engineering, The University of Sheffield, Sir Frederick Mappin Building, Mappin Street, Sheffield, S1 3JD, UK. i.hajirasouliha@sheffield.ac.uk

⁴ Senior Lecturer. Dept. of Civil and Structural Engineering, The University of Sheffield, Sir Frederick Mappin Building, Mappin Street, Sheffield, S1 3JD, UK. m.guadagnini@sheffield.ac.uk

⁵ Professor. Dept. of Civil and Structural Engineering, The University of Sheffield, Sir Frederick Mappin Building, Mappin Street, Sheffield, S1 3JD, UK. k.pilakoutas@sheffield.ac.uk

1
2
3
4
5
6
7
8
9
10
11
12
13
14
15
16
17
18
19
20
21
22
23
24
25
26
27
28
29
30
31
32
33
34
35
36
37
38
39
40
41
42
43
44
45
46
47
48
49
50
51
52
53
54
55
56
57
58
59
60
61
62
63
64
65

20 deformable concrete. The feasibility of utilising recycled rubber as aggregate in concrete has been assessed by many
21 studies in the past [1-4]. The majority of those investigations focused on compressive performance and found that
22 the replacement of mineral aggregates with rubber can reduce concrete density, workability, compressive strength
23 and elastic modulus. This means that rubberised concrete (RuC) can only be used for non-structural applications,
24 such as heat, sound and vibration isolation. More recently, it was also found that RuC has enhanced lateral strain [5,
25 6] under axial loading. This has led researchers during the EU-funded project “Anagenisi” [7] to confine rubberised
26 concrete (RuC) in an attempt to enhance axial strength and strain capacity [6]. The hypothesis was that confined
27 RuC could be used in regions with high deformation demands, such as base isolation columns and bridge bearings.
28 To model such elements, the full mechanical characteristics of RuC are required [8].

29 The compressive characteristics of RuC can be determined from uniaxial and triaxial compressive tests. However,
30 its tensile characteristics are difficult to obtain from direct tensile tests as the uneven distribution of rubber particles
31 results in a non-uniform distribution of tensile strength, even for small linear elements [1]. Hence, the tensile
32 performance of RuC is normally derived from splitting or flexural tensile tests. Experimental evidence [1, 5, 9] has
33 shown that the tensile strength (splitting or flexural) of RuC decreases with increasing rubber content. Furthermore,
34 the tensile strength values obtained from the two types of tests are not equivalent. The maximum strength derived
35 from flexural tests is governed by the concrete strength on the tension surface of the beam and can be affected by its
36 boundary and moisture conditions [10]. In the case of splitting tests, the majority of the concrete perpendicular to the
37 loading direction is under constant tensile stress, thus the splitting tensile strength is closer to the strength
38 determined from direct tensile tests [11]. On the other hand, flexural tests produce a more stable load-deflection
39 curve than splitting tests and can be used to obtain a more reliable estimate of the energy dissipation ability of RuC
40 after cracking [1]. Such test results prove that the flexural post-cracking performance of RuC is enhanced by the
41 replacement of aggregates with rubber particles [12]. This can be explained by the ability of rubber particles to store
42 elastic energy and dissipate it through pull-out [13]. Since both indirect tensile tests do not provide a direct measure
43 of the tensile stress-strain or stress-crack opening relations, there is a lack of a tensile constitutive model for this
44 novel material. This limits the development of numerical models that could demonstrate the applicability of RuC in
45 structural applications.

1
2
3
4 46 The Concrete Damage Plasticity (CDP) model is widely used to simulate the failure behaviour of concrete in finite
5
6 47 element analysis [14-16]. The CDP treats cracked concrete as a continuum and cracks are represented by cracking
7
8 48 strains smeared over a certain width of fracture zone, or the width of a finite element. Thus the constitutive
9
10 49 behaviour of cracked concrete is modelled using the stress-strain relations combined with a damage parameter [17].
11
12 50 The successful finite element modelling of RuC using CDP also requires the complete uniaxial tensile stress-strain
13
14 51 relationship. Although this cannot be obtained from direct tensile tests, it is possible to obtain the tensile stress-strain
15
16 52 relationship by inverse finite element analysis (FEA) on the flexural test result. However, if a softening material
17
18 53 model is only described on the basis of stress-strain relationships, strain-softening can lead to spurious sensitivity
19
20 54 with respect to the size of elements due to the localisation of deformation [17-19]. Mesh refinement leads to a
21
22 55 smaller strain localisation band width and reduces global energy dissipation. One remedy for this spurious mesh
23
24 56 sensitivity issue is to use the crack band technique [17, 20]. The basic idea of this technique is to modify the strain-
25
26 57 softening modulus to the chosen size of the finite element. This adjustment ensures that different size elements
27
28 58 dissipate identical fracture energies [21].

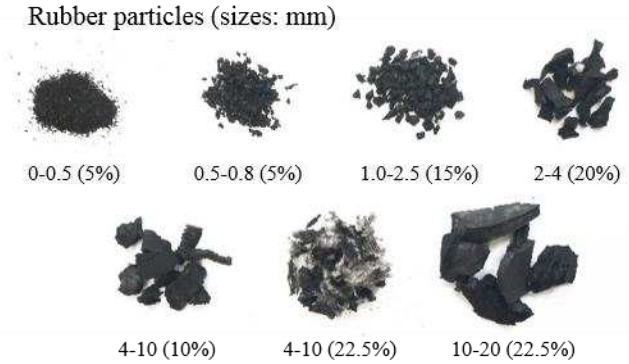
30
31
32 59 This study proposes a new tensile constitutive model for RuC obtained through inverse FEA and implemented in the
33
34 60 CDP model to predict the tensile behaviour of RuC. The paper initially describes an experimental program on which
35
36 61 three-point bending (TPB) and splitting tensile tests are utilised to determine the tensile behaviour of RuC. The next
37
38 62 sections describe the methodology applied for the inverse FEA and mesh sensitivity studies. Finally, to demonstrate
39
40 63 the efficiency of the proposed model, the predicted mechanical response using the proposed tensile σ - ε relationships
41
42 64 and relationships obtained from Model Code 2010 are compared. This work will lead to a better understanding of
43
44 65 the behaviour of RuC and will assist in developing applications for highly deformable elements.

48 66 **2. Experimental program**

49
50
51 67 Forty-five samples consisting of thirty-six cylindrical specimens ($\varnothing 100 \times 200$ mm) and nine prisms
52
53 68 (L500 \times W150 \times H150 mm) were manufactured to examine the compressive and tensile characteristics of RuC. The
54
55 69 samples were divided into three sets by rubber contents ($\rho_{vr} = 0\%$, 30% and 60%) and labelled as R0, R30 and R60,
56
57 70 respectively. The rubber content ρ_{vr} is defined as the volume of mineral aggregates in the reference regular concrete
58
59 71 mix replaced by rubber [5, 22].

1
2
3
4 **72 2.1 Rubber Particles**

5
6 **73** The recycled rubber particles were extracted from car (sizes up to 10 mm) and truck (sizes in the range of 10–20
7
8 **74** mm) end-of-life tyres [23]. Fig. 1 shows the particles size range and used ratio in the concrete mix. These
9
10 **75** proportions were adopted from an experimental study on RuC mixes conducted by Raffoul et al.[22], in which
11
12 **76** acceptable strength loss and desirable workability were achieved.



30 **78** Fig. 1. Rubber particles used in the concrete mix to replace sand (size:0-4 mm) and mineral aggregate (sizes: 4-10
31 **79** mm and 10-20 mm).

32
33 **80 2.2 Mix designs**

34
35
36 **81** A reference regular concrete mix ($\rho_{vr} = 0$) for bridge pier design with target 28-day compressive strength of 60 MPa
37
38 **82** was initially selected and modified for rubberised concrete mixing. In the RuC mixes, 20% of the cement (CEM II -
39
40 **83** 52.5N) was replaced by 50% fly ash [24] and 50% silica fume [25]. Silica fume and fly ash were added to increase
41
42 **84** flowability and strength and to improve particles packing. Two RuC mixes were produced with 30% and 60% of
43
44 **85** rubber contents, respectively. The specific gravity of mineral aggregates was considered to be 2.65, and that of
45
46 **86** rubber was 0.8 [22]. The quantities of rubber particles used in the mixes were 165 kg/m³ and 330 kg/m³,
47
48 **87** respectively. Table 1 summarises the mix proportions used in this study.

49
50 **88**
51
52 **89**
53
54 **90**
55
56 **91** Table 1. Mix proportions for optimised RuC mix.

ρ_{vr}	CEM	Silica	Pulverised	Aggregates	Rubber Particles	Plasticiser	Superplasticiser	Water	Designed
-------------	-----	--------	------------	------------	------------------	-------------	------------------	-------	----------

	II 52.5	Fume	Fuel Ash	kg/m ³			l/m ³			density	kg/m ³		
				0/5 mm	5/10 mm	10/20 mm	0/4 mm	4/10 mm	10/20 mm				
0	340	42.5	42.5	820	364	637	-	-	-	2.5	5.1	150	2396
30%	340	42.5	42.5	574	255	456	74	17	75	2.5	5.1	150	2026
60%	340	42.5	42.5	328	146	255	149	33	148	2.5	5.1	150	1634

2.3 Test procedure and methodology

2.3.1 Compressive and Splitting tests

The compressive (see Fig. 2a) and splitting tests (see Fig. 2b) on cylindrical specimens were conducted under load control at loading rates of 0.4 MPa/s [26] and 0.01 MPa/s [27], respectively. For the compressive tests, three laser sensors (accuracy of 0.005 mm) were used to measure global axial displacement. The sensors were mounted radially at 120° on two aluminium rings with 100 mm gauge length. Local axial strains were measured by using strain gauges placed at mid-height of the specimen. The possible initial rotations were accommodated by a top loading plate fitted with a hinge. The dimensions of each specimen were measured before testing. The specimen ends were strengthened with post-tensioned metal straps with a thickness of 0.8 mm and a width of 25 mm to avoid local failure.



Fig. 2. View of testing for a) Compression tests and b) Splitting tests.

The splitting tensile strength ($f_{ct,sp}$) can be calculated by Eq. (1) considering the maximum load (P_{max}) [27]:

$$f_{ct,sp} = \frac{2P_{max}}{\pi L d_{cy}} \quad (1)$$

where L is the length of the specimen, d_{cy} is the diameter of the cylinder.

1
2
3
4 107 The load in Eq. (1) is assumed to be concentrated along a line. However, the load is practically applied on a sheet of
5
6 108 plywood or compact cardboard. Rocco et al. [28] showed that the loading area width (t) can affect the tensile
7
8 109 strength of the cylinders up to 25%. Tang et al. [29] proposed the following equation to consider the effect of the
9
10 110 loading area width on the splitting tensile strength.

$$f_{ct,sp} = \frac{2P_{max}}{\pi L d_{cy}} \left(1 - \left(\frac{2t}{d_{cy}} \right)^2 \right)^{1.5} \quad (2)$$

11 112 Bompa et al. [5] proposed Eqs. (3) to predict the splitting tensile strength ($f_{ct,sp}$), tensile strength (f_{ct}) and elastic
12
13
14
15
16
17
18
19 112 modulus (E_c) as a function of the compressive strength (f_{co}) of RuC. The performance of these equations will be
20
21 113 evaluated against the test data obtained in this study.
22
23 114

24
25
26
27
28 115

$$\begin{aligned} f_{ct,sp} &= 0.26 f_{co}^{2/3} \\ f_{ct} &= 0.24 f_{co}^{2/3} \\ E_c &= 12 \left(\frac{f_{co}}{10} \right)^{2/3} \end{aligned} \quad (3)$$

29
30
31
32
33

34 116 2.3.2 Three-point bending tests

35
36 117 Before testing, the geometrical dimensions of each specimen were measured and a 5mm wide and 25 mm deep
37
38 118 notch was sawn at mid-span of the prisms and perpendicular to the cast surface using a diamond blade [30]. All
39
40 119 specimens were tested under a TPB loading arrangement using a 300 kN electromagnetic testing machine (see Fig.
41
42 120 3). Two Linear Variable Differential Transducers (LVDTs) were mounted on an aluminium yoke to measure central
43
44 121 deflections [31] and a clip gauge was mounted across the notch to obtain the crack mouth opening displacement
45
46 122 (CMOD) [32]. In order to achieve a stable result, the tests were CMOD-controlled at a constant rate of 0.02 mm/min
47
48 123 [33]. The load, central deflection and CMOD were recorded throughout loading history.
49
50
51
52
53
54
55
56
57
58
59
60
61
62
63
64
65

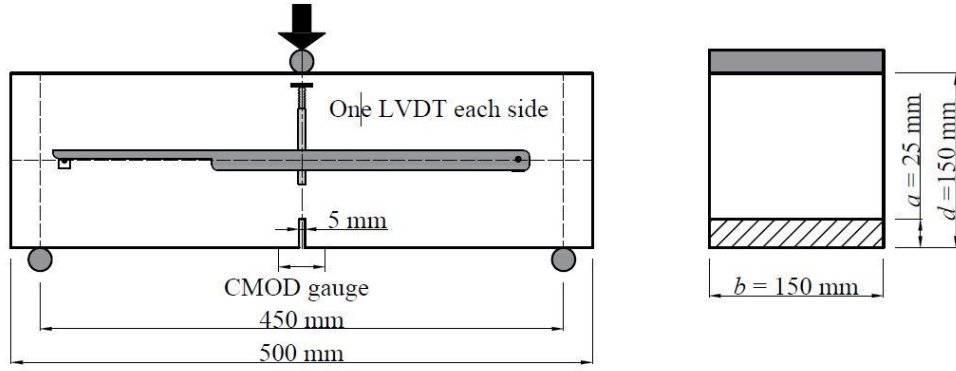


Fig. 3. Set-up of the three-point bending tests.

The flexural tensile strength ($f_{ctm,fl}$) can be calculated as the equivalent elastic tensile flexural stress corresponding to the maximum load recorded, as:

$$f_{ctm,fl} = \frac{3P_{max}l}{2b(d-a)^2} \quad (4)$$

where l is the span of the prism, b is the width of the prism, d is the depth of the prism, and a is the effective depth of the notch.

The flexural modulus of elasticity (E_{fm}) is determined by using the elastic flexural deformations, as given below:

$$E_{fm} = \frac{l^3 P}{48I\delta} \quad (5)$$

where P/δ (N/mm) is the slope of the load-deflection curve at 40% of the peak load and I (mm^4) is the second moment of area of the mid-span cross-section.

2.3.3 Total fracture energy using work-of-fracture method

Hillerborg's work-of-fracture method assumes that the energy required for crack formation is equivalent to the work of the external load. Thus the complete load-deflection curve of the specimen is necessary to estimate the work of the external load, which can be represented as the area under the load-deflection curve. The fracture energy (G_F) can be then calculated using the following equation [34]:

$$G_F = \frac{W_0 + \left(m_1 \frac{l}{L} + 2m_2\right) g \delta_0}{A_f} \quad (6)$$

where W_0 is energy absorption capacity, which represents the area under the load-deflection curve during the bending test; m_1 is the mass of the beam between supports; m_2 is the mass of the unattached loading apparatus; L and l are the length and span of the specimen, respectively; g is the gravity acceleration; δ_0 represents the maximum recorded deflection; and $A_f = (d - a)b$ denotes the area of the fracture surface.

2.4. Experimental results

2.4.1 Changes in unit weight

As a result of the low unit weight of rubber particles, the unit weight of rubberised concrete reduces by increasing the rubber content. Fig. 4 shows the expected linear relationship between unit weight (d_{RuC}) and rubber contents (ρ_{vr}). Compared with the unit weight of concrete mixes without rubber, the average unit weight of the concrete mix with a rubber content of 30% and 60% decreased by 15.4% and 31.8%, respectively.

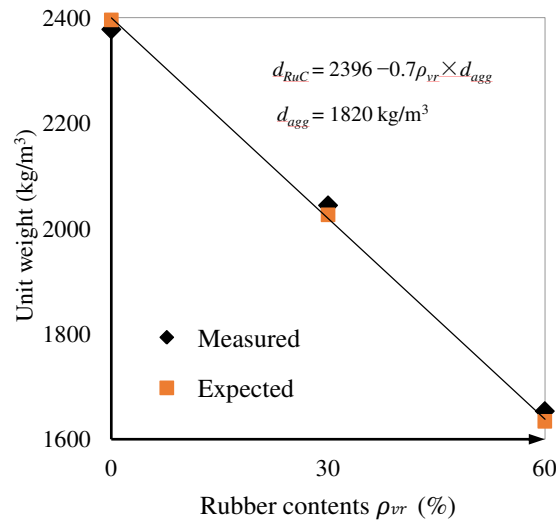


Fig. 4. Unit weight of RuC with different rubber contents ρ_{vr} .

2.4.2 Compressive and splitting tensile strength

The compressive test results are summarised in Table 2. The mean cylindrical compressive strengths (f_{co}) of R30 and R60 were about 29% and 10% of that of regular concrete R0 (75 MPa), respectively. The compressive stress-strain

curves are shown in Fig. 5. The elastic moduli (E_c) of R30 and R60 were 41% and 21% of that of R0 (41 GPa), respectively. The post-peak behaviour was also significantly influenced by the percentage of rubber content. The typical compressive failure patterns for the tested cylinders are shown in Fig. 6a. As expected, all plain ($\rho_{vr} = 0\%$) specimens failed suddenly in a brittle manner. The failure of RuC cylinders with $\rho_{vr} = 30\%$ and 60% was more gradual as the cylinders developed a large number of macro-cracks prior to failure. Rubber particles dilate more at lower displacements than mineral aggregates due to their high Poisson's ratio and low modulus of elasticity. This dilation generates internal splitting tensile stresses perpendicular to the loading direction and causes the concrete to fail at an earlier stage.

Table 2. Experimental results of examined concrete mixes

ρ_{vr}	f_{co} MPa	E_c GPa	$f_{ct,sp}$ MPa	$f_{ctm,fl}$ MPa	E_{fm} GPa	G_F N/mm	W_0 N·m
0	75 (5.6)	41 (2.3)	4.1 (0.32)	5.9 (0.5)	44 (9)	0.12 (0.02)	2.2 (0.02)
30	21.9 (3.6)	17 (3.5)	1.8 (1.29)	3.9 (1.86)	20 (8)	0.46 (0.14)	8.1 (0.14)
60	7.7 (0.3)	8.5 (1.2)	0.9 (0.52)	2.1 (0.22)	10 (0.3)	0.93 (0.06)	16.8 (0.06)

Note: Standard Deviation is presented in brackets.

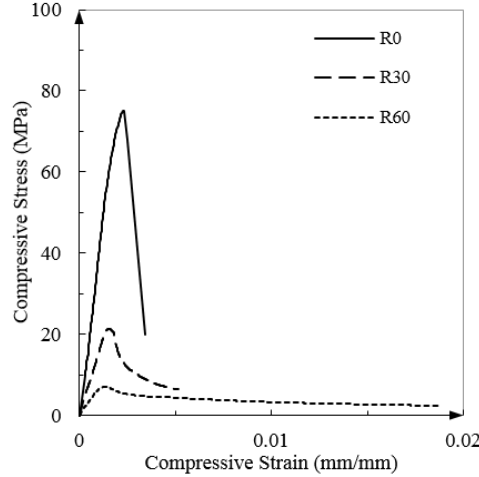
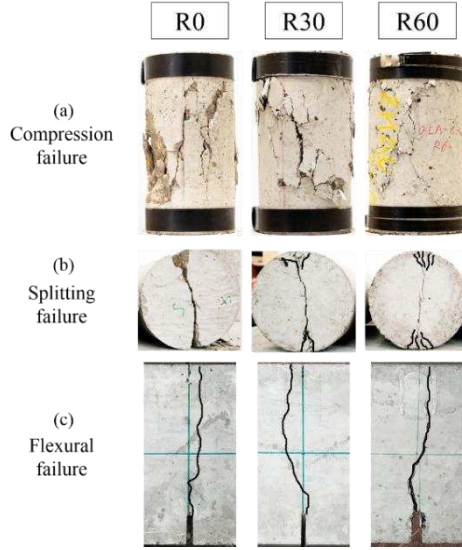


Fig. 5. Compressive stress-strain curves of R0, R30 and R60.



168

169 Fig. 6. Typical failure modes for a) Compression; b) Splitting tension and c) Flexural.

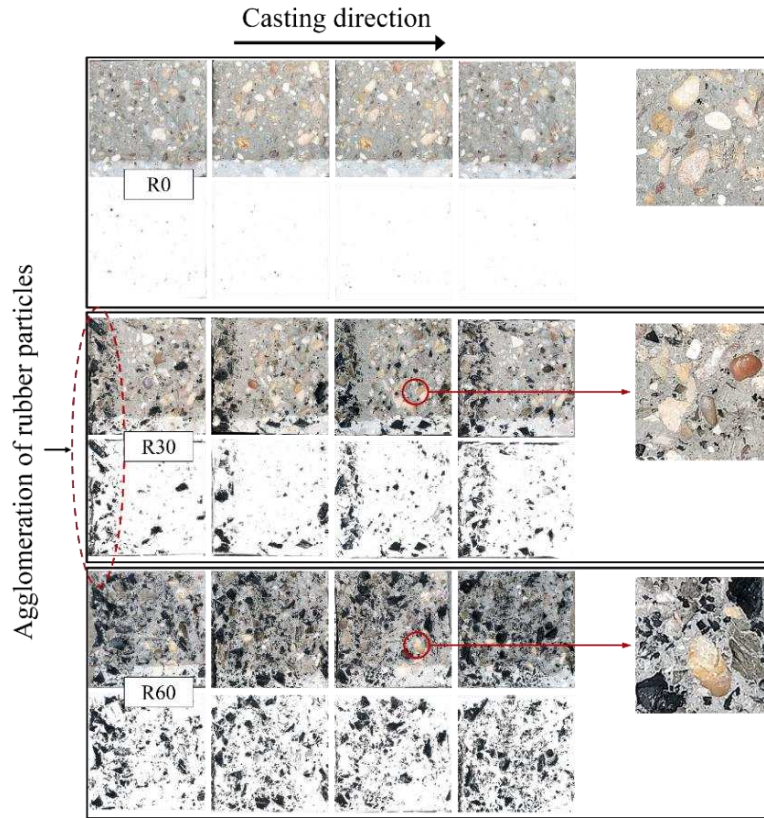
170 During the splitting tests, as expected, all samples failed due to wedge formation and splitting as shown in Fig. 6b.

171 Compared to the brittle failure mode of plain concrete, the RuC samples exhibited a slower axial splitting process
 172 and higher capacity in absorbing plastic energy. The regular concrete specimens split into two halves immediately
 173 upon reaching their ultimate load capacity, while the RuC specimens were capable of withstanding at least 80% of
 174 the ultimate load for about 30 seconds (R30) and 55 seconds (R60) after splitting. The RuC specimens underwent
 175 large displacements before the loading stopped, and the deformation was partially recovered upon unloading. All the
 176 RuC specimens maintained their integrity even for highly cracked specimens. The splitting tensile strength ($f_{ct,sp}$)
 177 results are reported in Table 2, which show an apparent degradation in tensile strength with increasing rubber
 178 content. However, the trend in tensile strength loss is less severe than in compressive strength. The splitting tensile
 179 strengths of R30 and R60 were 44% and 22% of that of R0 (4.1 MPa), respectively.

180 2.4.3 Three-point bending tests

181 The flexural failure patterns of all specimens are shown in Fig. 6c. The average flexural strength ($f_{cm,fl}$) and modulus
 182 (E_{fm}) of three replicates are listed in Table 2. Fig. 7 shows images of typical fracture surfaces obtained after the
 183 bending tests (upper row for each mix) as well as the results from the digital image processing of these sections
 184 (lower row) to examine rubber particle distribution along the casting direction. The images show that the rubber
 185 tended to float towards the cast face (left in the pictures) during vibration of the fresh concrete leading to an

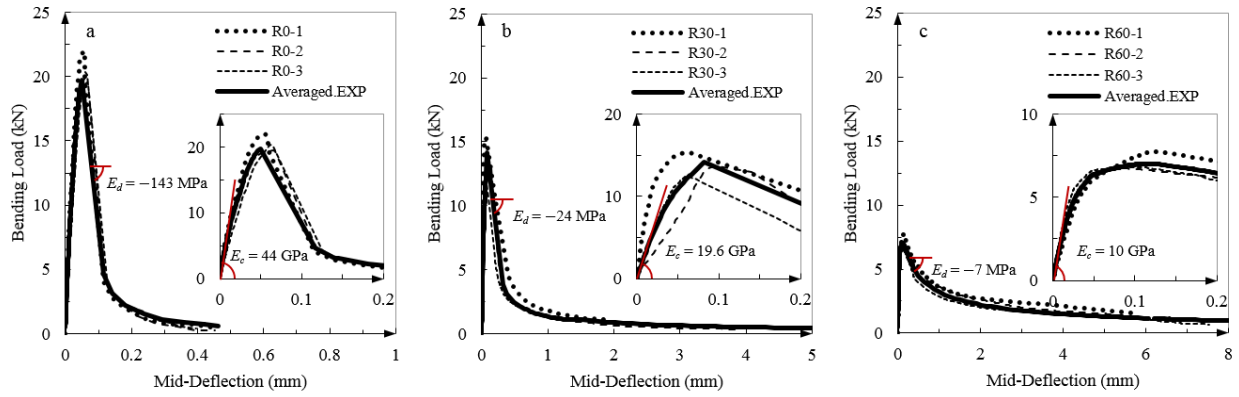
186 agglomeration of rubber particles. However, this tendency is less obvious in the specimens with a rubber content of
 187 $\rho_{vr} = 60\%$.



189 Fig. 7. The fracture surface of three-point bending tests.

190 Fig. 8 shows the individual and average $P-\delta$ curves from three TPB specimens for each of the ρ_{vr} tested. The mid-
 191 span deflection of each prism was determined by averaging the measurements from LVDTs. The response of the
 192 TPB test can be described by three typical phases: 1) an elastic phase up to cracking; 2) a short flexural hardening
 193 response up to the maximum flexural capacity; and 3) a reduction of the load with increasing CMOD/deflection. The
 194 comparative assessment of load-deflection curves from Fig. 8 shows a reduction in flexural strength and stiffness
 195 with increasing rubber content. The flexural strengths ($f_{cm,\eta}$) of concrete with $\rho_{vr} = 30\%$ and 60% are 66% and
 196 35.6% of the reference concrete, respectively. The flexural modulus (E_{fm}) of R30 and R60 were reduced to 45% and
 197 20% of that of R0, respectively. However, the ratio of cracking stress to flexural strength ($f_{cr}/f_{cm,\eta}$) are 54% , 68%
 198 and 72% for R0, R30 and R60, respectively. At load levels close to the peak, RuC specimens exhibited a stable
 199 transition from the pre-cracking to post-cracking regimes, while the reference (plain concrete) beams showed a

1
2
3
4 200 brittle behaviour after the maximum capacity was reached. Beyond the peak, the descending branch showed
5
6 201 reducing gradients ($E_{d,R0} = -143$, $E_{d,R30} = -24$ and $E_{d,R60} = -7$ MPa) and increasing energy absorption capacity ($W_0 =$
7
8 202 2.2; $W_{0,R30} = 8.1$ and $W_{0,R60} = 16.8$ N·m) and fracture energy ($G_{F,R0} = 0.15$, $G_{F,R30} = 0.51$ and $G_{F,R60} = 0.93$ N/mm²) as
9
10 203 the rubber content increased (see Fig .9). This enhancement indicates that the capability of rubberised concrete in
11
12 204 energy absorption is significantly better than regular concrete and RuC specimens developed up to 20 times larger
13
14 205 deflections. The higher deformability of rubberised concrete elements can potentially result in more resilient
15
16 206 structural systems and improve structural integrity under extreme load conditions.



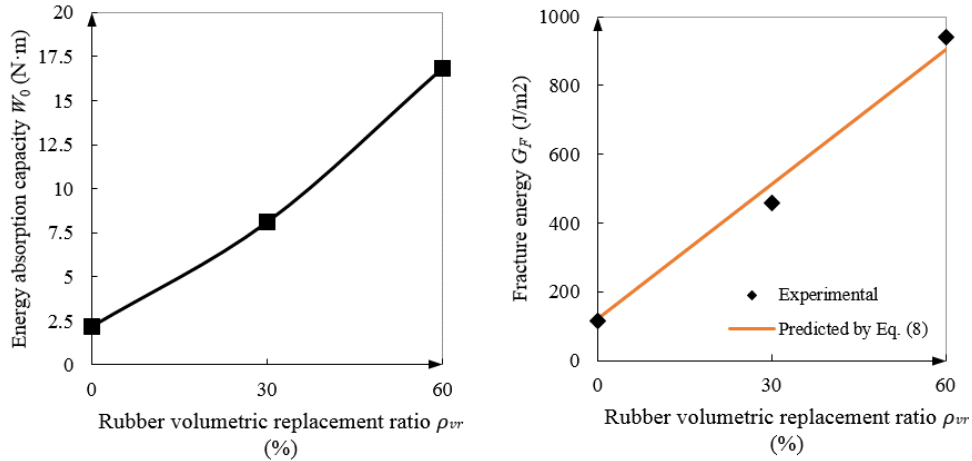
207
208 Fig. 8. Load-deflections of TPB specimens: (a) R0, (b) R30 and (c) R60.

209 The fracture energy (G_F) in N/mm² for regular concrete can be determined using Model Code 2010 [35]:

$$G_F = 0.073 \times f_{co}^{0.18} \quad (7)$$

210
211 Using the results of this study, a parametric equation was developed to calculate the fracture energy ($G_{F,RuC}$) of RuC
212 based on Eq. (7) and as a function of rubber content (ρ_{vr}) (Eq. (8) and Fig. 9):

$$G_{F,RuC} = (1 + 10.8\rho_{vr}) \cdot G_F \quad (8)$$



214

215 Fig. 9. Energy absorption capacity and fracture energy with different rubber contents.

216 Further inspection of the fractured surfaces (see Fig. 6) revealed a different degree of roughness depending on the
 217 percentage of rubber volume replacement. At 0% rubber replacement, almost all the aggregates were found broken.
 218 The flexural failure mode of RuC can be explained as follows. At 30% rubber replacement, the majority of mineral
 219 aggregates were found broken on the fracture surface. At 60% rubber replacement, no broken mineral aggregates
 220 were found on the fracture surface. When a tension crack propagates through RuC and reaches a rubber particle, the
 221 crack keeps developing in the same direction as the rubber has the ability to withstand large elastic deformation
 222 under small tensile stress. As rubber can withstand much higher tensile stress and strain until failure than cement and
 223 mineral aggregates, the primary failure mechanism of rubber particles is pull-out. This failure mechanism results in
 224 the energy dissipation enhancement discussed above.

225 3. Inverse FEA

226 Inverse fracture energy based FEA is developed and utilised in this section to obtain the tensile stress-strain curves
 227 of RuC by using the experimental results presented in Section 2.

228 3.1 Assumptions:

229 The following assumptions are used, the first three proposed by Uchida et al. [36]

- 230 i. A single main crack exists through a fracture area (see Fig. 10). A rotational axis exists on the top of the
 231 fracture area. The distribution of the crack opening is linear.

1
2
3
4
5
6
7
8
9
10
11
12
13
14
15
16
17
18
19
20
21
22
23
24
25
26
27
28
29
30
31
32
33
34
35
36
37
38
39
40
41
42
43
44
45
46
47
48
49
50
51
52
53
54
55
56
57
58
59
60
61
62
63
64
65

- 232 ii. The mean crack opening (w_c) at the fracture area is represented by half of the crack mouth opening displacement (CMOD) at the notch. This opening can be smeared over a crack band width to obtain strain.
- 234 iii. The externally applied energy is equivalent to the energy needed for crack development.
- 235 iv. The shape of the uniaxial tension softening curve of concrete is exponential, and the function proposed by Krätzig and Pölling [37] can be adopted (Eq. (9)):

$$y = e^{-\frac{\epsilon_{cr} x}{\gamma_t}} \quad (x > 1) \tag{9}$$

238 where $x = \epsilon_{ck}/\epsilon_{cr}$, $y = \sigma_t/f_{ct}$; σ_t and ϵ_{ck} are tensile stress and strain, respectively; ϵ_{cr} is cracking strain; the tensile strength (f_{ct}), and elastic modulus (E_c) can be calculated by Eqs. (3); γ_t adjusts the area under the stress-strain curve and can be determined by:

$$\gamma_t = \frac{g_t}{f_{ct}} - \frac{1}{2} \frac{f_{ct}}{E_c} \tag{10}$$

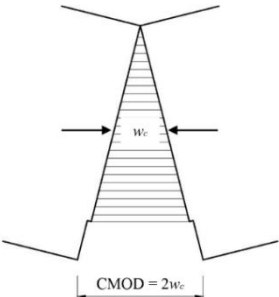


Fig. 10. Model of fracture area reproduced from Uchida et al. [33]

3.2 Definitions:

- $G_{ch} = w_{cb} \times g_c$ is energy dissipated during crushing in a compressive test;
- $G_F = w_{cb} \times g_t$ is energy required for crack propagation in a flexural test;
- Coefficients g_c and g_t are equal to the areas under $\sigma-\epsilon^p$ curves in uniaxial tension and compression, respectively, as shown in Fig. 11;

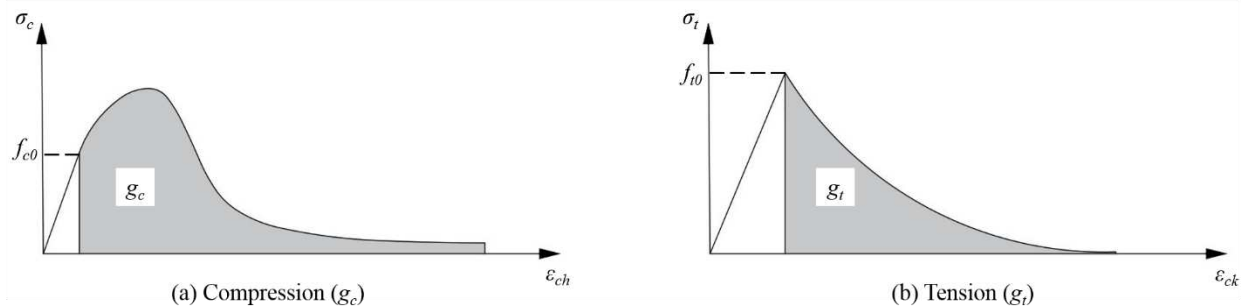


Fig. 11. Definition of coefficient g_c and g_t , after [8].

- w_{cb} is the crack band width of a heterogeneous material and represents the effective width of the strain-softening damage zone [38, 39]. This length can be expressed as the ratio of the energy dissipated per unit area (N/mm^2) to the energy dissipated per unit volume (N/mm^3).

Bazant and Oh [18] claimed that w_{cb} is approximately 2.7-3 times the maximum aggregate size d_a . The value of w_{cb} is also dependent on concrete strength. By reducing the difference between the elastic modulus of the coarse aggregates and the mortar (e.g. in high strength concrete), the value of w_{cb}/d_a decreases and a more homogeneous material is obtained. The opposite is expected for low strength concrete or when rubber aggregates are used as the material becomes more heterogeneous.

Since direct tensile tests on rubberised concrete are neither easy to perform nor available, the crack band width cannot be calculated via G_F / g_t . However, it can be estimated through the determination of the σ_c - ϵ_{ch} curve and crushing energy (G_{ch}) of RuC with various rubber contents from carefully instrumented compressive tests according to [8]. For the RuC mix examined, compressive test results are available from this study and Raffoul et al. [6], and an analytical σ - ϵ model is given by Bompa et al. [5]. These results are used to determine w_{cb} as shown in Table 3. It is interesting to note that the value of w_{cb} is higher for RuC and increases with increasing rubber content, which confirms the hypothesis that w_{cb} increases with increasing heterogeneity.

Table 3. Crushing energy (G_{ch}) and coefficient (g_t) of concrete with different rubber contents (ρ_{vr})

ρ_{vr}	G_{ch} N/mm^2	g_c N/mm^3	ϵ_{ult} mm/mm	g_t N/mm^3	w_{cb} / d_a
0	9.1	0.16	0.006	0.0027	2.8
30%	8.7	0.11	0.055	0.0065	3.9
60%	10.5	0.10	0.075	0.0088	5.0

Note: d_a is maximum aggregate size, which is 20 mm in this study.

3.3 Steps for the Inverse FEA

1. Determination of total external work (W_0) through the integration of the load-deflection curve.
2. Determination of fracture energy (G_F) by Eq. (6). Table 2 shows the results.
3. Determination of the ultimate cracking strain (ε_{ult}) of concrete by dividing the ultimate mean crack mouth opening ($w_{c,ult}$) by w_{cb} . Results are shown in Table 3.

$$\varepsilon_{ult} = \frac{w_{c,ult}}{w_{cb}} \quad (11)$$

4. Determination of g_t by using the fracture energy (G_F) obtained from bending tests. Results are shown in Table 3.

$$g_t = \frac{G_F}{w_{cb}} \quad (12)$$

5. Determination of the shape factor γ_t in Eq. (10) by using g_t . Results are shown in Fig. 12.

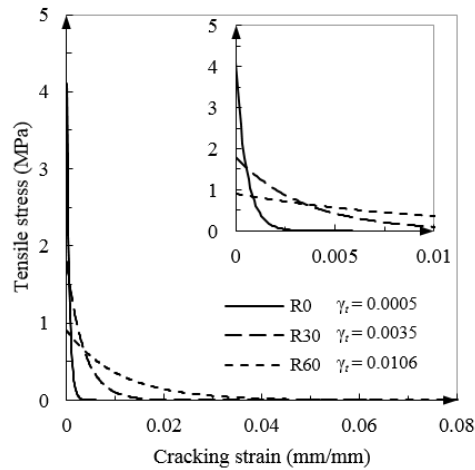


Fig. 12. Tensile stress-strain curves for concrete with various rubber contents.

4. Numerical modelling

A finite element model has been developed using Abaqus/Standard finite element software package [40]. The “Concrete Damaged Plasticity (CDP)” [41] developed by Lubliner et al. [8] and elaborated by Lee and Fenves [42]

1
2
3
4
5
6
7
8
9
10
11
12
13
14
15
16
17
18
19
20
21
22
23
24
25
26
27
28
29
30
31
32
33
34
35
36
37
38
39
40
41
42
43
44
45
46
47
48
49
50
51
52
53
54
55
56
57
58
59
60
61
62
63
64
65

283 is adopted as it allows the use of a custom tensile stress-strain model for concrete in tension. CDP uses the modified
284 Drucker-Prager criterion and the yield surface F in the deviatoric plane and assumes isotropic damage d . The details
285 can be found in [43].

286 The CDP model requires the following material functions and parameters:

- 287 • Stress-strain relations for uniaxial behaviour in compression and tension. The compressive stress-strain
288 relations proposed by Bompa et al. [5] are adopted in this study, and the tensile stress-strain relations are
289 obtained through inverse FEA (see Fig. 12).
- 290 • The damage variables d_c and d_t represent the portion of normalised energy dissipation for damage in
291 compression and tension, respectively [8]. The values of d_c and d_t are determined using Eqs. (13), and the
292 curves of d_t vs ε_{ck} are shown in Fig. 13 (zero means no damage and one means fully damaged).

$$d_c = \int_0^{\varepsilon_{ch}} \sigma_c d\varepsilon_{ch} / g_c; d_t = \int_0^{\varepsilon_{ck}} \sigma_t d\varepsilon_{ck} / g_t \quad (13)$$

- 294 • The default values of 2/3, 0.1 and 1.16 are assigned to shape parameter K_c , eccentricity ϵ , and the biaxial to
295 uniaxial compressive strength ratio f_{bo}/f_{co} , respectively [40]. A low viscosity parameter of 2×10^{-6} was used
296 to avoid convergence problems. It should be noted that the non-associative plastic volume deformation of
297 the concrete is controlled by the dilation angle ψ , while the lateral dilation of concrete increases with
298 increasing ψ . As replacing the mineral aggregates with rubber particles can dramatically increase the lateral
299 dilation of RuC by up to 300% over the plain concrete [6], a relatively high dilation angle $\psi = 40^\circ$ was
300 chosen for RuC [44, 45].

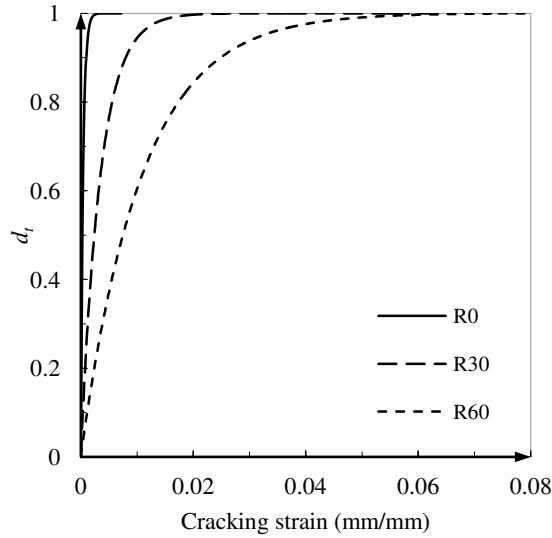


Fig. 13. Tensile damage variables (d_t) vs cracking strain (ε_{ck}).

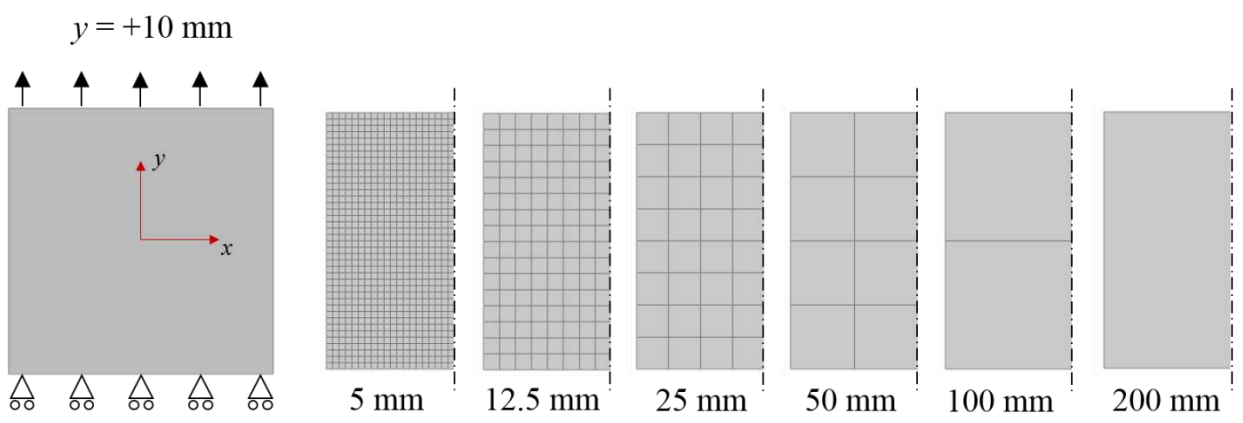
4.1 Mesh-sensitivity study

The lower bound value of finite element size that can be attributed to w_{cb} is shown in Table 3, while an upper bound value of $G_F E_c J_f^2$ is recommended by Bažant and Oh [38]. It can be seen that the lower bound values are significantly larger when compared with the dimension of the specimens examined in this study, thus to obtain a detailed resolution within the strain-softening region, the element mesh size (h_e) needs to be smaller than the experimentally derived w_{cb} . However, as discussed before, this would lead to mesh sensitivity issues as the dissipation of energy depends on the width of the element size used in the area where the damage is localised. To investigate the mesh-sensitivity problem, the numerical response of a square plate (200×200 mm) subjected to plane stress conditions (Fig. 14) was examined. A monotonically increasing displacement in the positive y -direction was applied to the upper boundary ($y = +10$ mm), while a traction-free boundary condition was applied to the bottom edge. The numerical calculation was performed using four-node elements with four integration points (CPS4) and six different mesh sizes (see Fig. 14). The reduced integration option was not considered in this study as it is not reliable for problems involving crack formation [46]. The tensile stress-strain relation of R60 with a value of $w_{cb} = 100$ mm was used.

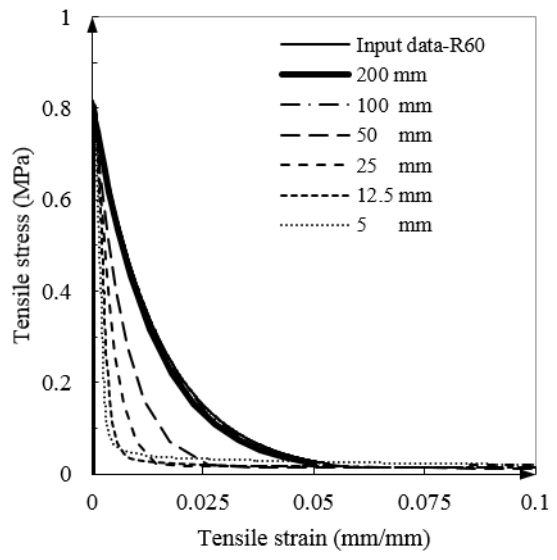
Fig. 15 illustrates the average resulting stress on the upper boundary vs average tensile strain, which clearly shows the sensitivity of the results to the selected mesh size. It can be noted that only the stress-strain curves obtained from

1
2
3
4
5
6
7
8
9
10
11
12
13
14
15
16
17
18
19
20
21
22
23
24
25
26
27
28
29
30
31
32
33
34
35
36
37
38
39
40
41
42
43
44
45
46
47
48
49
50
51
52
53
54
55
56
57
58
59
60
61
62
63
64
65

319 the plate with the element sizes above 100 mm are similar to the curves derived from the input data (i.e.
320 experimental test results). Fig. 16 shows that the total energy dissipation is mesh-dependent as a result of the
321 localisation of deformations (see Fig. 16).



322
323 Fig. 14. Plate subjected to uniaxial tension: boundary conditions and examined mesh geometries.



324
325 Fig. 15. Tensile response of a plate subjected to uniaxial tension and modelled using different mesh sizes.

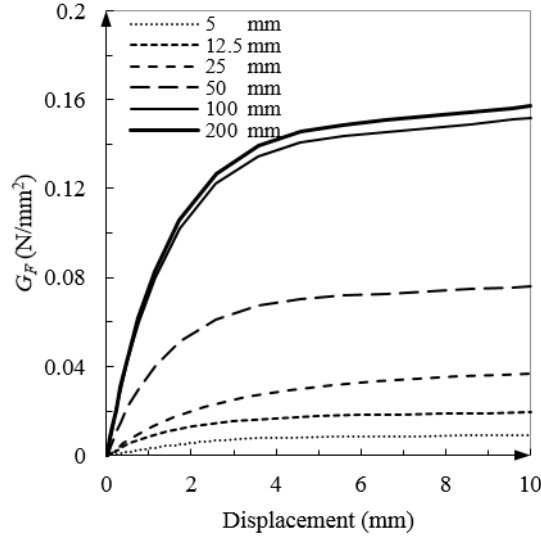


Fig. 16. Total energy dissipation of a plate subjected to uniaxial tension and modelled using different mesh sizes.

4.2 Modified procedure

Based on the numerical observation above, the element mesh size (h_e) used in the fracture zone should be carefully selected when defining the tensile behaviour of the material. The crack band model can provide substantially the same results regardless of the width of the strain localisation zone when the energy dissipation per unit area of the crack band plane is correct [17]. The softening modulus of the post-peak softening curve can be adjusted by incorporating the ratio of element size (h_e) to the crack band width (w_{cb}) so that the correct energy dissipation per unit crack surface can be obtained for all cases. In a uniaxial tensile experiment on concrete, the dissipated energy (G_F) per unit crack surface can be written as

$$G_F = w_{cb} \left[\int_0^{\varepsilon_{ult}} e^{-\frac{\varepsilon_{cr}}{\gamma_t}} d\varepsilon_{cr} \right] = h_e \left[\int_0^{\varepsilon_{ult, h_e}} e^{-\frac{\varepsilon_{cr}}{\gamma_{t, h_e}}} d\varepsilon_{cr} \right] \quad (14)$$

The shape factor γ_{t, h_e} for different mesh sizes can be obtained as:

$$\gamma_{t, h_e} = \lambda \frac{g_t}{f_{ct}} - \frac{1}{2} \frac{f_{ct}}{E_c} \quad (15)$$

Hence, the corresponding ultimate cracking strain is:

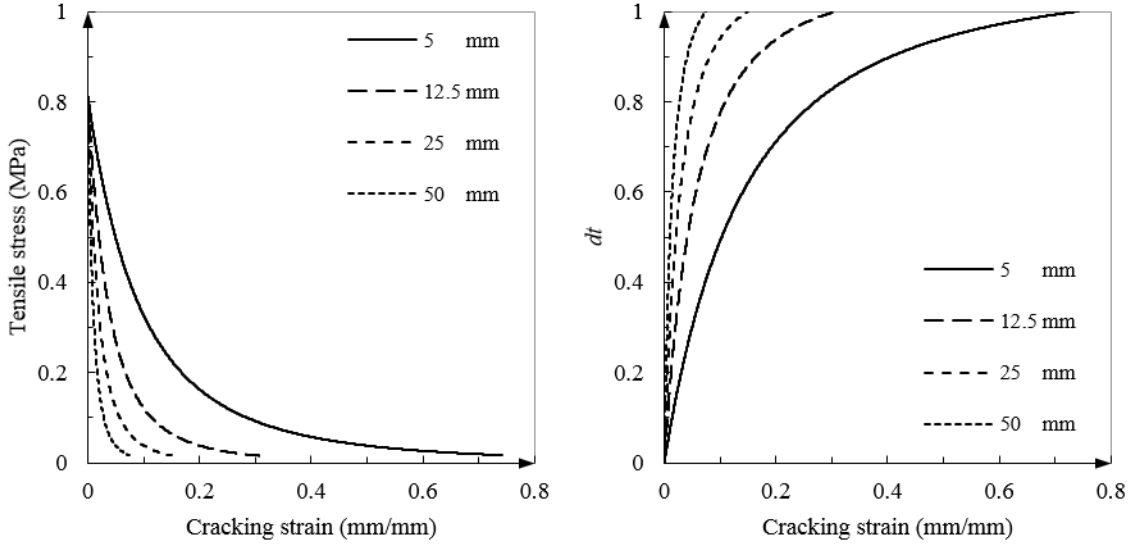
1
2
3
4
5
6
7
8
9
10
11
12
13
14
15
16
17
18
19
20
21
22
23
24
25
26
27
28
29
30
31
32
33
34
35
36
37
38
39
40
41
42
43
44
45
46
47
48
49
50
51
52
53
54
55
56
57
58
59
60
61
62
63
64
65

340
$$\varepsilon_{ult,h_e} = \lambda \varepsilon_{ult} \tag{16}$$

341 where $\lambda = w_{cb}/h_e$. h_e is the element size. For a square element with a surface area A_e , the value of h_e is equal to $\sqrt{A_e}$.

342 A detailed discussion on element size can be found in [20, 47].

343 The modified tensile stress/damage variable vs cracking strain curves of R60 for different mesh sizes are shown in
344 Fig. 17. The effectiveness of the modification expressed by Eqs. 16 and 17 are illustrated in Fig. 18, which confirms
345 that similar total energy dissipation can be obtained with different mesh sizes.



346
347 Fig. 17. Modified tensile constitutive laws of R60 for different mesh sizes: (a) tensile stress-cracking strain curves;
348 (b) damage variables-cracking strain curves.

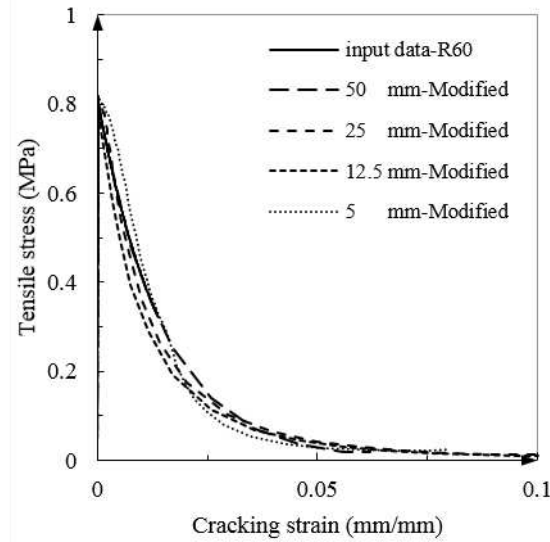


Fig. 18. Results of the modified tensile constitutive laws of R60 with respect to different mesh sizes under uniaxial tensile loading.

The proposed methodology enables the derivation of a more reliable tensile constitutive law for both conventional and rubberised concrete solely based on values obtained from simple compression tests. Eqs. (3) and (7) or (8) can be used to calculate tensile strength (f_{ct}) and fracture energy (G_f), respectively; while the crack band width (w_{cb}) of rubberised concrete tested in this study was found to be directly proportional to the rubber content (ρ_{vr}). A linear relationship between w_{cb}/d_a and ρ_{vr} ($w_{cb}/d_a = 3.67\rho_{vr} + 2.8$) was found to capture reasonably well the crack band width variation for the concrete tested in this study, but further work should be carried out to validate these findings for different values of ρ_{vr} or different particles size distributions. For any given mesh size (h_e), the complete tensile constitutive law can be described by Eqs. (14 - 16).

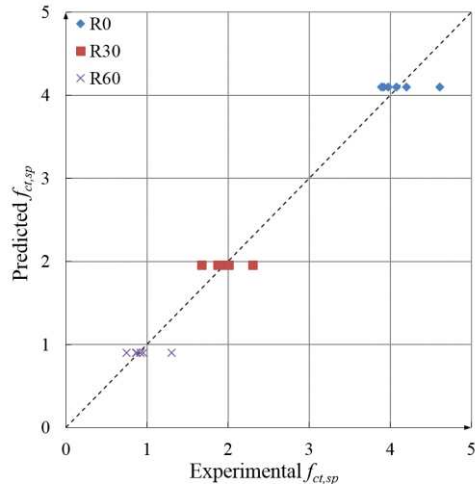
4.3 Verification of the material model

4.3.1 Splitting tests

Finite element modelling of cylinders subjected to splitting tests was performed to examine whether Eqs. (3) can provide a reasonable prediction of the splitting tensile strength. As the diametric compression load was applied experimentally through a plywood strip (width: 10 mm and thickness: 3 mm), the same area was used to apply the load on the surface of the cylinder in the numerical analysis. Since maximum capacity is mesh-independent, an

1
2
3
4
5
6
7
8
9
10
11
12
13
14
15
16
17
18
19
20
21
22
23
24
25
26
27
28
29
30
31
32
33
34
35
36
37
38
39
40
41
42
43
44
45
46
47
48
49
50
51
52
53
54
55
56
57
58
59
60
61
62
63
64
65

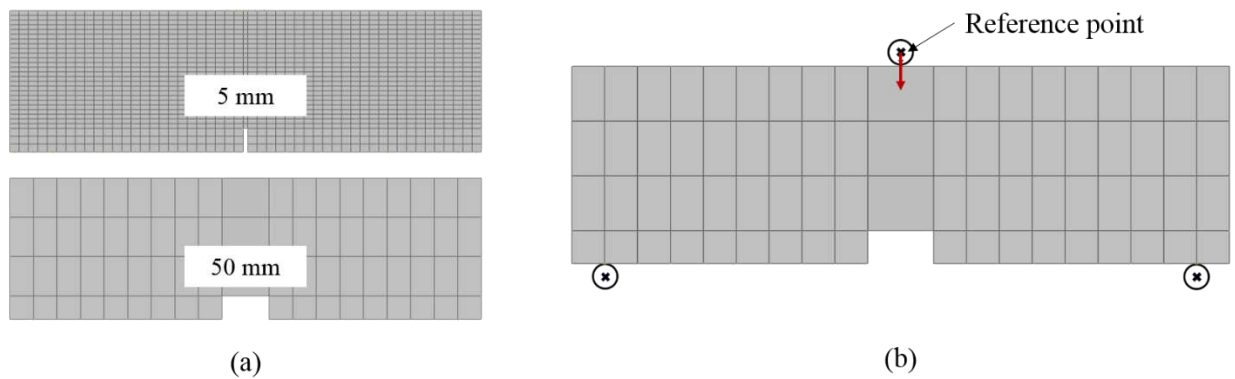
366 arbitrary mesh size of 15 mm was chosen [20]. Fig. 19 shows the comparison between numerical and experimental
367 results, which confirms the effectiveness of Eqs. (3).



369 Fig. 19. Comparison of the predicted splitting tensile strength with experimental results.

370 4.3.2 TPB tests

371 Two finite element meshes (5 mm and 50 mm in fracture area) were used to model the beams subjected to TPB, as
372 illustrated in Fig.20a. In the TPB tests, the load was applied via a steel roller. In the numerical study, the steel roller
373 was modelled as a rigid body and a load was applied as a displacement at the relative reference point (see Fig. 20b).
374 A frictionless surface-to-surface interaction was assigned to the steel roller-concrete interface.



375
376 Fig. 20. Discretisation of a beam subjected to a three-point bending test.

1
2
3
4
5
6
7
8
9
10
11
12
13
14
15
16
17
18
19
20
21
22
23
24
25
26
27
28
29
30
31
32
33
34
35
36
37
38
39
40
41
42
43
44
45
46
47
48
49
50
51
52
53
54
55
56
57
58
59
60
61
62
63
64
65

377 For each rubber content, the load-deflection curves were calculated by using the general stress-strain relations
 378 suggested by Model Code 2010 [35] and by the proposed model with the adaptable softening modulus (obtained
 379 from inverse FEA). The Model Code stress-strain relation was derived from the bilinear stress-crack opening
 380 relation accounting for the selected mesh size (h_e) as follows:

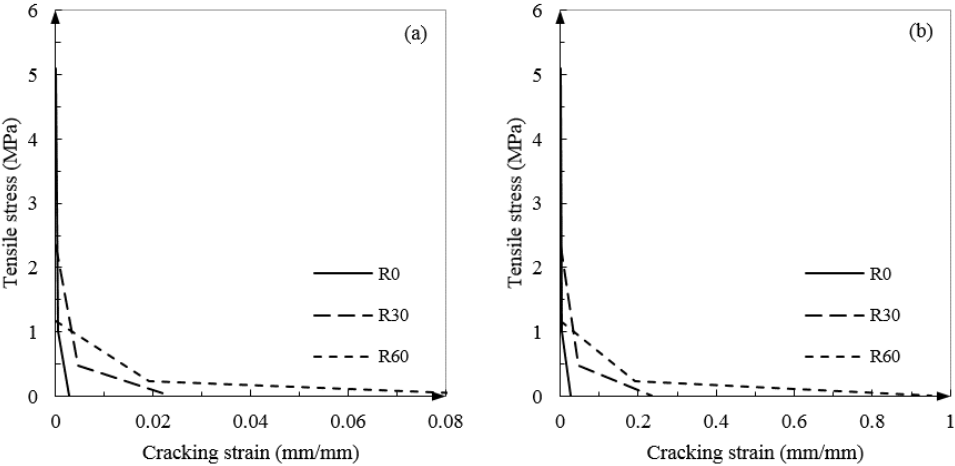
$$\begin{aligned} \sigma_t &= f_{ct} \cdot (1.0 - 0.8 \cdot \frac{w}{w_1}) && \text{for } w \leq w_1 \\ \sigma_t &= f_{ct} \cdot (0.25 - 0.05 \cdot \frac{w}{w_1}) && \text{for } w_1 < w \leq w_c \end{aligned} \tag{17}$$

382 where $w_1 = G_F/f_{ct}$ is the crack opening at $\sigma_t = 0.2f_{ct}$, $w_2 = 5G_F/f_{ct}$ is the crack opening at $\sigma_t = 0$ and $f_{ct} = 0.3(f_{co})^{2/3}$.

383 Fig. 21 shows the converted tensile stress-strain curves for mesh sizes 50 mm and 5 mm, respectively. The accuracy
 384 of the two models was evaluated by the errors in the FE predictions for peak load and energy absorption capacity as
 385 well as the Mean Square Error (MSE) between the predicted load-deflection behaviour over the entire loading range
 386 and the corresponding experimental results (average of three tests).

$$MSE = \frac{\sum_{i=1}^N [(\chi)_i^{anal} - (\chi)_i^{exp}]^2}{N} \tag{18}$$

388 where $(\chi)_i^{anal}$ represents the predicted values of flexural load ($f_{cm,\beta}$), $(\chi)_i^{exp}$ shows the corresponding experimental
 389 values and N is the total number of collection data.



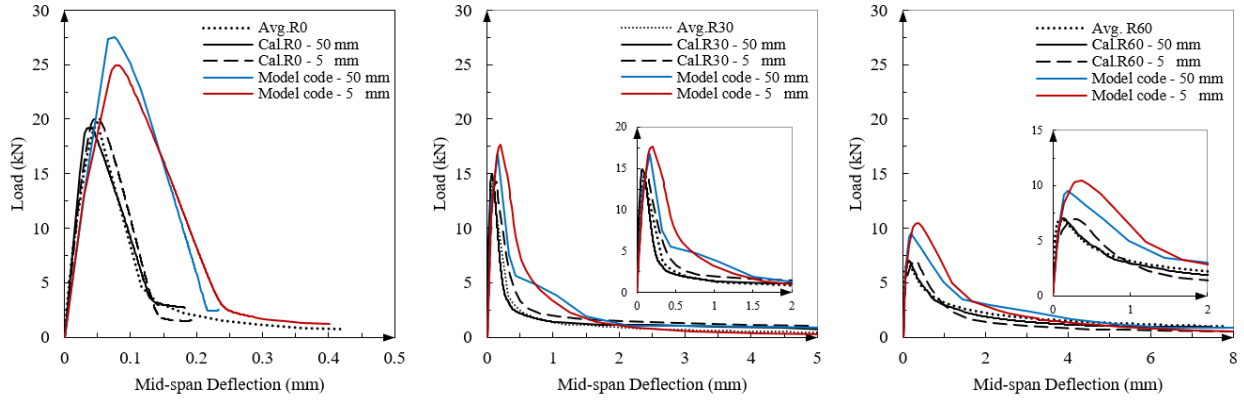
391 Fig. 21. Stress-strain curves according to Model Code 2010: (a) mesh size 50 mm; (b) mesh size 5 mm

1
2
3
4
5
6
7
8
9
10
11
12
13
14
15
16
17
18
19
20
21
22
23
24
25
26
27
28
29
30
31
32
33
34
35
36
37
38
39
40
41
42
43
44
45
46
47
48
49
50
51
52
53
54
55
56
57
58
59
60
61
62
63
64
65

392 In Fig. 22, the average experimental load-deflection curves for all tested TPB specimens are compared with the
393 numerical predictions. It is shown that the numerical analyses performed using the inverse FEA stress-strain
394 relations show a considerably better agreement with the experimental data for both rubberised and conventional
395 concrete specimens. It can be seen that when the Model Code relations are adopted, higher flexural strength is
396 obtained, as well as larger fracture energy. This can be attributed to the fact that the bilinear stress-strain curve of
397 Model Code yields a higher value for the coefficient g_t (see Fig. 23). Moreover, the load-deflection curve obtained
398 from implementing the proposed relations with different mesh sizes can achieve nearly identical results, thus
399 confirming that proposed relations describe more accurately the evolution of g_t at increasing levels of strain.

400 For better comparison, the calculated errors are also summarised in Table 4. The results indicate that the stress-strain
401 relation recommended in Model Code led to, on average, 32% and 63% overestimation of the peak flexural load and
402 the energy absorption capacity, respectively. It should be mentioned that similar observations were reported in [48,
403 49]. However, by using the modified stress-strain relation with adaptable softening modulus, the average errors
404 reduced to 11% and 3% for energy absorption capacity and peak flexural load, respectively. The MSE results also
405 confirm that the proposed adaptive stress-strain relation can provide an accurate simulation of the flexural behaviour
406 of concrete over the entire loading range.

407 Fig. 24 shows the variation of the damage parameter (d_t) vs CMOD for R0, R30 and R60. The value of d_t for the
408 reference concrete R0 increases rapidly for relatively small CMOD values due to the relative low toughness and
409 higher brittleness of regular concrete. The d_t of RuC (R30 and R60), however, increases at a slower rate once the
410 crack develops, and the severity of damage evolution decreases with increasing rubber content. This can be
411 attributed to the fact that the rubber particles can control crack development and lead to an increase in ultimate
412 CMOD and overall ductility.



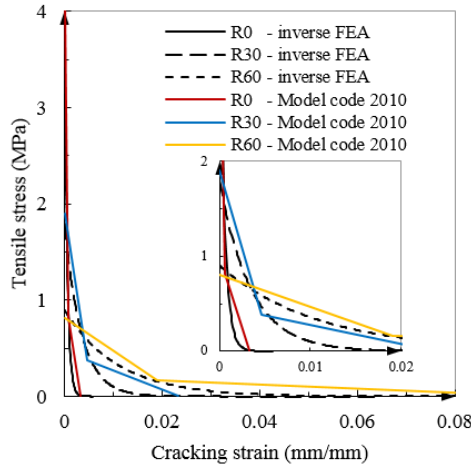
413

414 Fig. 22. Comparison of numerically derived load-deflection curves with experimental data.

415 Table 4. Errors in predicting load-deflection response, peak load and energy absorption.

h_e (mm)	ρ_{vr} (%)	Error in peak load		Error in energy absorption		MSE of load-deflection response	
		MC 2010	Inverse FEA	MC 2010	Inverse FEA	MC 2010	Inverse FEA
5	R0	26%	2.6%	70%	10%	78%	1.7%
	R30	25%	5.6%	58%	17%	21%	2.4%
	R60	49%	0.2%	50%	16%	9%	0.8%
50	R0	39%	2.6%	67%	13%	95%	1.3%
	R30	19%	5.8%	83%	3%	18%	1.1%
	R60	35%	0.3%	49%	8%	4%	0.3%

416



417

418 Fig. 23. Comparison of stress-strain curves for Model Code 2010 and modified model obtained based on inverse
419 FEA.

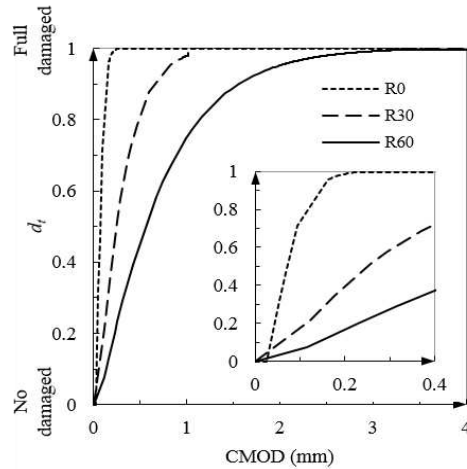


Fig. 24. Evolution of the damage variable, d_t .

5. Conclusions

In this paper, the fracture energy of rubberised concrete has been investigated by conducting three-point bending tests. The primary parameter investigated was the total aggregate replacement volume by rubber particles. The experimental results show that replacing mineral aggregates with rubber particles leads to an apparent reduction in strength (compressive, tensile and flexural) and elastic modulus. However, a less severe reduction is observed in the tensile and flexural properties. Replacing aggregates with rubber also enhanced the fracture energy and energy absorption capacity and led to a more ductile post-cracking behaviour. The test results enabled the implementation of an energy-based inverse finite element analysis method to obtain the tensile stress-strain relation of rubberised concrete indirectly. The proposed constitutive laws were implemented in the concrete damage plasticity model in ABAQUS to analyse the tensile strain-softening behaviour numerically. The influence of mesh size on load-displacement and energy dissipation was examined and an adaptive method was proposed to eliminate mesh dependency by introducing element size and fracture energy as parameters in the tensile constitutive model. It is shown that the proposed methodology can provide significantly more accurate predictions compared to the implementation of the strain-softening relationship proposed in Model Code 2010 for regular concrete in terms of peak load, energy absorption capacity and load-deflection response over the entire loading range.

1
2
3
4
5
6
7
8
9
10
11
12
13
14
15
16
17
18
19
20
21
22
23
24
25
26
27
28
29
30
31
32
33
34
35
36
37
38
39
40
41
42
43
44
45
46
47
48
49
50
51
52
53
54
55
56
57
58
59
60
61
62
63
64
65

Acknowledgements

The study contributes to the FP7 EU-funded project “Anagennisi” [FP7/2007- 2013] under grant agreement n° 603722. The first author also appreciates the support from China Scholarship Council (CSC) under Grant CSC n° 201608060059.

References

- [1] N.N. Eldin, A.B. Senouci, Rubber-tire particles as concrete aggregate, *Journal of materials in civil engineering*, 5(4) (1993) 478-496.
- [2] I.B. Topcu, The properties of rubberized concretes, *Cement and Concrete Research*, 25(2) (1995) 304-310.
- [3] R. Siddique, T.R. Naik, Properties of concrete containing scrap-tire rubber—an overview, *Waste Management*, 24(6) (2004) 563-569.
- [4] Z.K. Khatib, F.M. Bayomy, Rubberized Portland cement concrete, *Journal of materials in civil engineering*, 11(3) (1999) 206-213.
- [5] D. Bompa, A. Elghazouli, B. Xu, P. Stafford, A. Ruiz-Teran, Experimental assessment and constitutive modelling of rubberised concrete materials, *Construction and Building Materials*, 137 (2017) 246-260.
- [6] S. Raffoul, R. Garcia, D. Escolano-Margarit, M. Guadagnini, I. Hajirasouliha, K. Pilakoutas, Behaviour of unconfined and FRP-confined rubberised concrete in axial compression, *Construction and Building Materials* 147 (2017) 388-397.
- [7] K. Pilakoutas, S. Raffoul, P. Papastergiou, R. Garcia, M. Guadagnini, I. Hajirasouliha, Innovative reuse of all tyre components in concrete: the Anagennisi project, *Proc. of the International Conference on Sustainable Structural Concrete*, 2015, pp. 15-18.
- [8] J. Lubliner, J. Oliver, S. Oller, E. Onate, A plastic-damage model for concrete, *International Journal of solids and structures* 25(3) (1989) 299-326.
- [9] A. Payne, J. Scott, The properties, testing and design of rubber as an engineering material, MacLaren & Sons, LTD, London, UK and Interscience Publishers, Inc, 1960.
- [10] S. Carmona, A. Aguado, New model for the indirect determination of the tensile stress–strain curve of concrete by means of the Brazilian test, *Materials and Structures* 45(10) (2012) 1473-1485.
- [11] C. Ozyildirim, N.J. Carino, Concrete strength testing, Significance of Tests and Properties of Concrete and Concrete-Making Materials, ASTM International, 2006.
- [12] A. Turatsinze, M. Garros, On the modulus of elasticity and strain capacity of self-compacting concrete incorporating rubber aggregates, *Resources, conservation and recycling* 52(10) (2008) 1209-1215.
- [13] M.M. Reda Taha, A. El-Dieb, M. Abd El-Wahab, M. Abdel-Hameed, Mechanical, fracture, and microstructural investigations of rubber concrete, *Journal of materials in civil engineering* 20(10) (2008) 640-649.
- [14] W. Brekelmans, J. De Vree, Reduction of mesh sensitivity in continuum damage mechanics, *Acta Mechanica* 110(1-4) (1995) 49-56.
- [15] L. Kachanov, *Introduction to continuum damage mechanics*, Springer Science & Business Media 2013.
- [16] J.-L. Chaboche, *Continuum damage mechanics: Part II—Damage growth, crack initiation, and crack growth*, *Journal of applied mechanics* 55(1) (1988) 65-72.
- [17] J.G. Rots, P. Nauta, G. Kuster, J. Blaauwendraad, Smeared crack approach and fracture localization in concrete, (1985).
- [18] Z.P. Bažant, B.H. Oh, Crack band theory for fracture of concrete, *Matériaux et construction* 16(3) (1983) 155-177.
- [19] J. Červenka, Z.P. Bažant, M. Wierer, Equivalent localization element for crack band approach to mesh - sensitivity in microplane model, *International Journal for Numerical Methods in Engineering* 62(5) (2005) 700-726.
- [20] J.G. Rots, *Computational modeling of concrete fracture*, 1988.
- [21] Z.P. Bažant, Concrete fracture models: testing and practice, *Engineering Fracture Mechanics* 69(2) (2002) 165-205.
- [22] S. Raffoul, R. Garcia, K. Pilakoutas, M. Guadagnini, N.F. Medina, Optimisation of rubberised concrete with high rubber content: An experimental investigation, *Construction and Building Materials* 124 (2016) 391-404.
- [23] N.F. Medina, R. Garcia, I. Hajirasouliha, K. Pilakoutas, M. Guadagnini, S. Raffoul, Composites with recycled rubber aggregates: Properties and opportunities in construction, *Construction and Building Materials* 188 (2018) 884-897.
- [24] CEN (European Committee for Standardization) EN 450-1:2012 Fly ash for concrete – Part 1: definition, specifications and conformity criteria. CEN, Brussels (Belgium), 2012.

- 1
2
3
4 501 [25] ELKEM, Elkem Microsilica Grade 940 for Concrete, [https://www.elkem.com/ silicon-materials/high-](https://www.elkem.com/silicon-materials/high-performance-concrete/microsilica-concrete-grades/microsilica-grade-940-construction/)
5 502 [performance-concrete/microsilica-concrete-grades/](https://www.elkem.com/silicon-materials/high-performance-concrete/microsilica-concrete-grades/microsilica-grade-940-construction/) [microsilica-grade-940-construction/](https://www.elkem.com/silicon-materials/high-performance-concrete/microsilica-concrete-grades/microsilica-grade-940-construction/).
- 6 503 [26] ASTM International. C39/C39M - 15 Standard Test Method for Compressive Strength of Cylindrical Concrete
7 504 Specimens, West Conshohocken (USA), 2015.
- 8 505 [27] ASTM International. C496/C496M - 11 Standard Test Method for Splitting Tensile Strength of Cylindrical
9 506 Concrete Specimens, West Conshohocken (USA), 2015.
- 10 507 [28] C. Rocco, G.V. Guinea, J. Planas, M. Elices, Size effect and boundary conditions in the Brazilian test:
11 508 experimental verification, *Materials and Structures* 32(3) (1999) 210.
- 12 509 [29] T. Tang, S.P. Shah, C. Ouyang, Fracture mechanics and size effect of concrete in tension, *Journal of Structural*
13 510 *Engineering* 118(11) (1992) 3169-3185.
- 14 511 [30] Institution BS. Test Method for Metallic Fibre Concrete: Measuring the Flexural Tensile Strength (limit of
15 512 Proportionality (LOP), Residual): BSI, 2008.
- 16 513 [31] N. Banthia, J.-F. Trottier, Test methods for flexural toughness characterization of fiber reinforced concrete:
17 514 some concerns and a proposition, *ACI Materials Journal* 92 (1995) 48-48.
- 18 515 [32] CEN. Test method for metallic fiber concrete—Measuring the flexural tensile strength (limit of proportionality
19 516 (LOP), residual), 2012.
- 20 517 [33] B. Barr, M. Lee, E.J. de Place Hansen, D. Dupont, E. Erdem, S. Schaerlaekens, B. Schnütgen, H. Stang, L.
21 518 Vandewalle, Round-robin analysis of the RILEM TC 162-TDF beam-bending test: part 1—test method evaluation,
22 519 *Materials and Structures* 36(9) (2003) 609-620.
- 23 520 [34] R.D. Recommendation, Determination of the fracture energy of mortar and concrete by means of three-point
24 521 bend tests on notched beams, *Materials and Structures* 18(106) (1985) 285-290.
- 25 522 [35] Model Code, fib Model Code for Concrete Structures. KGaA, Weinheim, Germany: Wiley-VCH Verlag GmbH
26 523 & Co., 2010. <http://doi.org/10.1002/9783433604090>.
- 27 524 [36] Y. UCHIDA, K. ROKUGO, W. KOYANAGI, Determination of tension softening curves of concrete by means
28 525 of bending tests, ECF8, Torino 1990.
- 29 526 [37] W.B. Krätzig, R. Pölling, An elasto-plastic damage model for reinforced concrete with minimum number of
30 527 material parameters, *Computers & Structures* 82(15-16) (2004) 1201-1215.
- 31 528 [38] Z.P. Bažant, G. Pijaudier-Cabot, Measurement of characteristic length of nonlocal continuum, *Journal of*
32 529 *engineering mechanics* 115(4) (1989) 755-767.
- 33 530 [39] J. Oliver, A consistent characteristic length for smeared cracking models, *International Journal for Numerical*
34 531 *Methods in Engineering* 28(2) (1989) 461-474.
- 35 532 [40] D. Systèmes, Abaqus analysis user's manual, Simulia Corp. Providence, RI, USA, 2007.
- 36 533 [41] Abaqus, Abaqus user manual (version 6.14), 2014.
- 37 534 [42] J. Lee, G.L. Fenves, Plastic-damage model for cyclic loading of concrete structures, *Journal of engineering*
38 535 *mechanics* 124(8) (1998) 892-900.
- 39 536 [43] D. Systèmes, Abaqus 6.14—Analysis Users's Guide: Volume IV: Elements, Providence, Rhode Island, 2013.
- 40 537 [44] O. Youssf, M.A. ElGawady, J.E. Mills, X. Ma, An experimental investigation of crumb rubber concrete
41 538 confined by fibre reinforced polymer tubes, *Construction and Building Materials* 53 (2014) 522-532.
- 42 539 [45] A. Duarte, B. Silva, N. Silvestre, J. de Brito, E. Júlio, Mechanical characterization of rubberized concrete using
43 540 an image-processing/XFEM coupled procedure, *Composites Part B: Engineering* 78 (2015) 214-226.
- 44 541 [46] R. De Borst, P. Nauta, Non-orthogonal cracks in a smeared finite element model, *Engineering Computations*
45 542 2(1) (1985) 35-46.
- 46 543 [47] L. Chen, R. de Borst, Cohesive fracture analysis using Powell - Sabin B - splines, *International Journal for*
47 544 *Numerical and Analytical Methods in Geomechanics* 43(2) (2019) 625-640.
- 48 545 [48] H. Hu, P. Papastergiou, H. Angelakopoulos, M. Guadagnini, K. Pilakoutas, Mechanical properties of SFRC
49 546 using blended manufactured and recycled tyre steel fibres, *Construction and Building Materials* 163 (2018) 376-389.
- 50 547 [49] H. Tlemat, K. Pilakoutas, K. Neocleous, Modelling of SFRC using inverse finite element analysis, *Materials*
51 548 *and Structures* 39(2) (2006) 221-233.
- 52 549
53
54
55
56
57
58
59 550
60
61
62
63
64
65

List of Figures

- Fig. 1. Rubber particles used in the concrete mix to replace sand (size:0-4 mm) and mineral aggregate (sizes: 4-10 mm and 10-20 mm).
- Fig. 2. View of testing for a) Compression tests and b) Splitting tests.
- Fig. 3. Set-up of the three-point bending tests.
- Fig. 4. Unit weight of RuC with different rubber contents ρ_{vr} .
- Fig. 5. Compressive stress-strain curves of R0, R30 and R60.
- Fig. 6. Typical failure modes for a) Compression; b) Splitting tension and c) Flexural.
- Fig. 7. The fracture surface of three-point bending tests.
- Fig. 8. Load-deflections of TPB specimens: (a) R0, (b) R30 and (c) R60.
- Fig. 9. Energy absorption capacity and fracture energy with different rubber contents.
- Fig. 10. Model of fracture area reproduced from Uchida et al. [33]
- Fig. 11. Definition of coefficient g_c and g_r after [8].
- Fig. 12. Tensile stress-strain curves for concrete with various rubber contents.
- Fig. 13. Tensile damage variables (d_t) vs cracking strain (ϵ_{ck}).
- Fig. 14. Plate subjected to uniaxial tension: boundary conditions and examined mesh geometries.
- Fig. 15. Tensile response of a plate subjected to uniaxial tension and modelled using different mesh sizes.
- Fig. 16. Total energy dissipation of a plate subjected to uniaxial tension and modelled using different mesh sizes.
- Fig. 17. Modified tensile constitutive laws of R60 for different mesh sizes: (a) tensile stress-cracking strain curves; (b) damage variables-cracking strain curves.
- Fig. 18. Results of the modified tensile constitutive laws of R60 with respect to different mesh sizes under uniaxial tensile loading.
- Fig. 19. Comparison of the predicted splitting tensile strength with experimental results.
- Fig. 20. Discretisation of a beam subjected to a three-point bending test.
- Fig. 21. Stress-strain curves according to Model Code 2010: (a) mesh size 50 mm; (b) mesh size 5 mm
- Fig. 22. Comparison of numerically derived load-deflection curves with experimental data.
- Fig. 23. Comparison of stress-strain curves for Model Code 2010 and modified model obtained based on inverse FEA.

1
2
3
4
5
6
7
8
9
10
11
12
13
14
15
16
17
18
19
20
21
22
23
24
25
26
27
28
29
30
31
32
33
34
35
36
37
38
39
40
41
42
43
44
45
46
47
48
49
50
51
52
53
54
55
56
57
58
59
60
61
62
63
64
65

579 Fig. 24. Evolution of the damage variable, d_t .

580 **List of Tables**

581 Table 1. Mix proportions for optimised RuC mix.

582 Table 2. Experimental results of examined concrete mixes

583 Table 3. Crushing energy (G_{ch}) and coefficient (g_t) of concrete with different rubber contents (ρ_{vr})

584 Table 4. Errors in predicting load-deflection response, peak load and energy absorption.

585

586

587